CFD Based Multi-Component Aerodynamic Optimization for Wing Propeller Coupling

Heyecan U. Koyuncuoglu* and Ping He[†] *Iowa State University, Ames, Iowa, 50011, USA*

Electric vertical take-off and landing (eVTOL) aircraft with distributed electric propulsion have received increasing interest in recent years because of their potential for zero-emission, on-demand air travel. The aerodynamic efficiency of wings and propellers has a significant impact on the eVTOL aircraft's overall performance. However, existing studies either optimized the wing and propeller separately or used low-fidelity models (e.g., blade element momentum and vortex lattice method) for wing-propeller coupled optimization. It is not clear to what extent high-fidelity coupled wing-propeller aerodynamic optimization can benefit propeller aircraft design. The objective of this paper is to develop the capability to simultaneously optimize the wing and propeller with high-fidelity models. We use computational fluid dynamics (CFD) solvers to simulate the wing and propeller aerodynamics with two separate meshes (components). We then use the discrete adjoint approach to compute the derivatives and couple them with a gradient-based optimization algorithm for handling a large number of design variables. The wing-propeller coupling is done by extracting the CFD propeller force and outer radius and adding the corresponding actuator source term into the CFD wing flow field under the OpenMDAO/MPhys framework. The objective function is the propeller power consumption, and the design variables are the wing shape and twist, propeller center, twist, chord, outer radius, and rotation speed. We impose a force balance constraint to ensure that the propeller thrust equals the wing drag. We also impose other aerodynamic and geometric constraints, such as lift, volume, and thickness for the wing. We obtain 18.3% power reduction for the coupled optimization and all constraints are satisfied. This study is expected to provide high-fidelity optimization results to facilitate the wing-propeller design for eVTOL aircraft.

I. Introduction

The powered flight history begins with the propeller aircraft. The first aircraft relied on piston engine-driven propellers to generate enough power to make flight possible. Aircraft propulsion systems are advanced during these 120 years, but propeller systems are still popular for aircraft flying at low speeds, such as light sport, general aviation, trainer, floatplane, amphibian, and firefighter aircraft. The most recent addition to these aircraft is NASA's electric-powered Advanced Air Mobility (AAM) concept [1], which has drawn increasing attention in recent years. This attention increase also caused an increasing interest in the design and optimization of electric propeller aircraft in the past decade [2–16]. The electric propulsion systems have many benefits like low emission, low maintenance cost, structural simplicity and most importantly allowing distributed propulsion systems [2]. The main advantages of distributed propulsion systems are facilitating vertical takeoff and landing (VTOL) and short takeoff and landing (STOL) capabilities and reducing aircraft size and takeoff weight. A well-known example of aircraft with distributed propulsion system is NASA's X-57 aircraft, which is optimized from a Tecnam P2006T. The X-57's cruise lift coefficient is nearly three times of the baseline wing, although its wing is 58% smaller than the baseline [6].

In recent years, many studies focusing on the aerodynamics of wing and propeller systems have been published [7, 9, 17–21]. However, the optimization studies among these studies either fixed the propeller and optimized the wing or isolated the wing and propeller and optimized them separately. Although coupled wing-propeller optimizations have been done in [7, 9, 17]; the wing and/or propellers were modeled by using low-fidelity methods, e.g., blade element momentum and vortex lattice method. In our previous study [22], we developed the capability to simultaneously optimize the wing shape and propeller parameters using high-fidelity computational fluid dynamics (CFD). We used a CFD solver to simulate the wing aerodynamics and the propeller was modeled as an actuator disk; CFD was not used for simulating the propeller. In this study, we extend our previous work by using high-fidelity CFD solvers to

^{*}PhD Student, Department of Aerospace Engineering, AIAA Student Member.

[†]Assistant Professor, Department of Aerospace Engineering, AIAA Senior Member. Email: phe@iastate.edu

simulate the wing and propeller with two separate meshes (components) for a tighter wing-propeller coupling. We then use the discrete adjoint approach to compute the derivatives and couple them with a gradient-based optimization algorithm for handling a large number of design variables. The wing-propeller coupling is done by extracting the CFD propeller force and outer radius and adding the corresponding actuator source term into the CFD wing flow field under the OpenMDAO/MPhys framework. We will conduct three high-fidelity aerodynamic optimizations, i.e., wing-only, propeller-only, and coupled wing-propeller, and analyze the optimization results.

The rest of this paper is organized as follows. In Section II, we elaborate on the multi-component aerodynamic analysis and optimization framework, followed by the detailed aerodynamic optimization results in Section III. Finally, in Section IV, conclusions are drawn, and perspectives and future improvements are provided.

II. Method

A. Steady-state turbulent flow simulation

The primal flow analyses are done by using our modified version of OpenFOAM's rhoSimpleFoam solver that solves 3D, steady-state turbulent flows governed by the compressible Navier-Stokes (NS) equations:

$$\nabla \cdot (\rho U_a) = 0 \tag{1}$$

$$\nabla \cdot (\rho U_r U_a) + \omega \times U_a + \nabla p - \nabla \cdot \mu_{\text{eff}} (\nabla U_a + \nabla U_a^T) = 0$$
 (2)

$$\nabla \cdot (\rho e U_a) + \nabla \cdot (0.5\rho |U|_a^2 U_a + p U_a) - \alpha_{\text{eff}} \nabla \cdot (\nabla e) - f \cdot U = 0$$
(3)

where U = [u, v, w] is the velocity vector, p is the pressure, ρ is the density, ω is the propeller rotational speed vector, $\mu_{\text{eff}} = \mu + \mu_t$ is the sum of dynamic viscosity and turbulent eddy viscosity, e is the internal energy, α_{eff} is the effective thermal diffusivity. The subscripts e and e of e denote the absolute and relative velocities, respectively, where e denote the absolute and relative velocities, respectively, where e denote the absolute and relative velocities, respectively, where e denote the absolute and relative velocities, respectively, where e denote the absolute and relative velocities, respectively, where e denote the absolute and relative velocities, respectively, where e denote the absolute and relative velocities, respectively, where e denote the absolute and relative velocities, respectively, where e denote the absolute and relative velocities, respectively, where e denote the absolute and relative velocities, respectively, where e denote the absolute and relative velocities, respectively, where e denote the absolute and relative velocities, respectively, where e denote the absolute and relative velocities, respectively, where e denote the absolute and relative velocities, respectively, where e denote the absolute and relative velocities, respectively.

The Spalart-Allmaras model is used to connect the turbulent eddy viscosity to the mean flow variables, which is explained in detail in their paper [23]:

$$\nabla \cdot (U_a \widetilde{v}) + \frac{1}{\sigma} \{ \nabla \cdot \left[(v + \widetilde{v}) \nabla \widetilde{v} \right] + C_{b1} |\nabla \widetilde{v}|^2 \} - C_{b1} \widetilde{S} \widetilde{v} + C_{w1} f_w \left(\frac{\widetilde{v}}{d} \right)^2 = 0$$
 (4)

Then, the semi-implicit method for pressure-linked equations (SIMPLE) [24] algorithm is extended to solve the compressible NS equations. After the discretization of momentum equation (2), an intermediate velocity field is solved using the pressure field from the previous iteration or an initial guess, p^0 .

$$a_P U_p + \sum_N a_N U_N = -\nabla p^0 + f \tag{5}$$

where a is the finite-volume discretization coefficient, the subscripts P and N denote the control volume cell and all neighboring cells, respectively. Rearranging the above equation, we get the following:

$$a_P U_p = -\sum_N a_N U_N + f - \nabla p^0 = H - \nabla p^0$$
(6)

where H represents the influence of all neighboring cells' velocities and the source term:

$$H = -\sum_{N} a_N U_N + f \tag{7}$$

The face flux, ϕ is introduced to linearize the convective term:

$$\int_{S} \rho U U \cdot dS = \sum_{f} U_{f} [\rho U_{f} \cdot S_{f}] = \sum_{f} \phi^{0} U_{f}$$
(8)

where the subscript f denotes the cell face, ϕ^0 denotes the face flux from the previous iteration or an initial guess.

An intermediate velocity field is obtained by solving the discretized momentum equation (6); however, this intermediate velocity field does not satisfy the continuity equation yet. To satisfy the continuity equation, a new pressure field is computed to correct the velocity field and face flux. Such that both the momentum and continuity equations are satisfied. The discretized continuity equation is:

$$\int_{S} \rho \mathbf{U} \cdot d\mathbf{S} = \sum_{f} [\rho \mathbf{U}]_{f} \cdot \mathbf{S}_{f} = 0$$
(9)

Here U_f is computed by interpolating the cell-centered velocity U_p , which is obtained from Eq. 6, onto the cell face:

$$[\rho \mathbf{U}]_f = \left(\frac{\rho \mathbf{H}}{a_p}\right)_f - \left(\frac{\rho}{a_p}\right)_f (\nabla p)_f \tag{10}$$

This momentum interpolation method is effective in mitigating the oscillating pressure issue, as proposed by Rhie and Chow [25]. A Poisson equation is obtained by substituting Eq. 10 into Eq. 9:

$$\nabla \cdot \left(\frac{\rho}{a_p} \nabla p^1\right) = \nabla \cdot \left(\frac{\rho \mathbf{H}}{a_p}\right) \tag{11}$$

By solving the above Poisson equation, we can obtain the updated pressure field p^1 and use it to update the face flux and the velocity field:

$$\phi^{1} = [\rho \mathbf{U}]_{f} \cdot \mathbf{S}_{f} = \left[\left(\frac{\rho \mathbf{H}}{a_{p}} \right)_{f} - \left(\frac{\rho}{a_{p}} \right)_{f} \left(\nabla p^{1} \right)_{f} \right] \cdot \mathbf{S}_{f}$$
(12)

$$U^{1} = \left(\frac{1}{a_{p}}\right) \left[\boldsymbol{H} - \nabla p^{1} \right] \tag{13}$$

By these, the velocity and pressure fields satisfy both continuity and momentum equations. After this, the density is updated using the new pressure and compressibility variable ($\psi = 1/RT$):

$$\rho = p\psi \tag{14}$$

Next, the energy equation (3) is solved to obtain the new internal energy e. Then, a Newton-Raphson (NR) method is used to solve the compressibility ψ based on the internal energy e. Finally, an updated turbulence viscosity, v_t , is obtained by solving Eq. (3). The above steps will be repeated until all the governing equations converge.

B. Discrete adjoint derivative computation

We use the discrete adjoint method to compute the derivatives for optimization. The function of interest is the function of both the design and state variables:

$$f = f(\mathbf{x}, \mathbf{w}) \tag{15}$$

where $x \in \mathbb{R}^{n_x}$ is the design variable vector, and $w^n \in \mathbb{R}^{n_w}$ is flow state variable vector. n_x and n_w are the number of design and state variables, respectively. The chain rule is applied to compute df/dx:

$$\left[\frac{\mathrm{d}f}{\mathrm{d}\mathbf{x}}\right]_{1\times n_{x}} = \left[\frac{\partial f}{\partial \mathbf{x}}\right]_{1\times n_{x}} + \left[\frac{\partial f}{\partial \mathbf{w}}\right]_{1\times n_{x}} \left[\frac{\mathrm{d}\mathbf{w}}{\mathrm{d}\mathbf{x}}\right]_{n_{x}\times n_{x}}$$
(16)

The partial derivatives in Eq. (16) only involve explicit computations, they are relatively cheap to calculate. However, the total derivative dw/dx is expensive because both terms are determined implicitly.

Similarly, the chain rule is applied to flow residual vector, $\mathbf{R} \in \mathbb{R}^{n_w}$, to solve the $d\mathbf{w}/d\mathbf{x}$ term. Because the governing equations have to be satisfied regardless of the values of design variables x, the total derivative $d\mathbf{R}/d\mathbf{x}$ must be zero:

$$\frac{\mathrm{d}\mathbf{R}}{\mathrm{d}\mathbf{x}} = \frac{\partial \mathbf{R}}{\partial \mathbf{x}} + \frac{\partial \mathbf{R}}{\partial \mathbf{w}} \frac{\mathrm{d}\mathbf{w}}{\mathrm{d}\mathbf{x}} = 0 \tag{17}$$

Substituting Eq. (17) into Eq. (16):

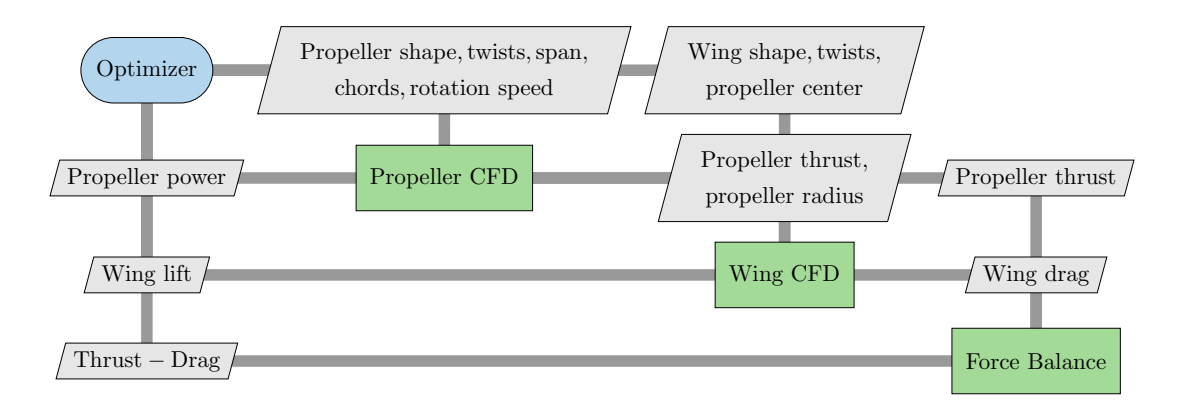


Fig. 1 Coupled wing-propeller optimization using OpenMDAO/MPhys. The optimizer minimizes the propeller power subject to constraints such as wing lift and force balance (wing drag equals the propeller thrust). We use the extended design structure matrix (XDSM) visualization standard where the diagonal blocks are components and the off-diagonal blocks are data transfer.

$$\left[\frac{\mathrm{d}f}{\mathrm{d}x}\right]_{1\times n_{x}} = \left[\frac{\partial f}{\partial x}\right]_{1\times n_{x}} - \left[\frac{\partial f}{\partial w}\right]_{1\times n_{w}} \left[\frac{\partial R}{\partial w}\right]_{n_{w}\times n_{w}}^{-1} \left[\frac{\mathrm{d}R}{\mathrm{d}x}\right]_{n_{w}\times n_{x}} = \left[\frac{\partial f}{\partial x}\right]_{1\times n_{x}} - \left[\psi^{T}\right]_{1\times n_{w}} \left[\frac{\mathrm{d}R}{\mathrm{d}x}\right]_{n_{w}\times n_{x}} \tag{18}$$

where ψ is the adjoint vector. Transposing the Jacobian and solve with $[df/dw]^T$ as the right-hand side yields the adjoint equations:

$$\left[\frac{\partial \mathbf{R}}{\partial \mathbf{w}}\right]_{n_w \times n_w}^T \cdot \left[\mathbf{\psi}\right]_{n_w \times 1} = \left[\frac{\partial f}{\partial \mathbf{w}}\right]_{n_w \times 1}^T \tag{19}$$

We can compute the total derivatives by substituting Eq. (19) into Eq. (16):

$$\frac{\mathrm{d}f}{\mathrm{d}\mathbf{x}} = \frac{\partial f}{\partial \mathbf{x}} - \boldsymbol{\psi}^T \frac{\partial \mathbf{R}}{\partial \mathbf{x}} \tag{20}$$

The adjoint equations are needed to solve only once for each function of interest because the design variables do not explicitly present in Eq. (19). The computational cost of it is independent of the number of design variables, but proportional to the number of objective functions. This approach, which is also known as the adjoint method, is advantageous for aerodynamic shape optimizations, which have only a few objective functions but numerous design variables.

In this study, the discrete adjoint derivative computation is based on an open-source, object-oriented adjoint framework DAFoam [26–28]. DAFoam uses a Jacobian-free adjoint approach, in which the partial derivatives and matrix-vector products are computed using the automatic differentiation, as detailed in Kenway et al. [29].

Finally, we use the generalized minimal residual (GMRES) iterative linear equation solver in the PETSc [30] library to solve the adjoint equation. A nested preconditioning strategy with the additive Schwartz method is used as the global preconditioner and the incomplete lower and upper (ILU) factorization approach with one level of fill-in for the local preconditioning. The preconditioner matrix $[\partial R/\partial w]_{RC}^T$ is constructed by approximating the residuals and their linearizations [26] to improve convergence. The construction of $[\partial R/\partial w]_{RC}^T$ is only done for the first time instance and then is reused for the adjoint equation. This treatment significantly reduces the adjoint runtime because the constructing $[\partial R/\partial w]_{RC}^T$ consists of ~30% of the adjoint runtime.

C. Coupling of high-fidelity wing and propeller CFD components

In this study, we demonstrate a high-fidelity multi-component framework for optimizing wing-propeller coupling based on the OpenMDAO/MPhys framework. OpenMDAO [31] is an open-source multidisciplinary design, analysis, and optimization framework developed by NASA. OpenMDAO has been widely used for large-scale aerospace engineering

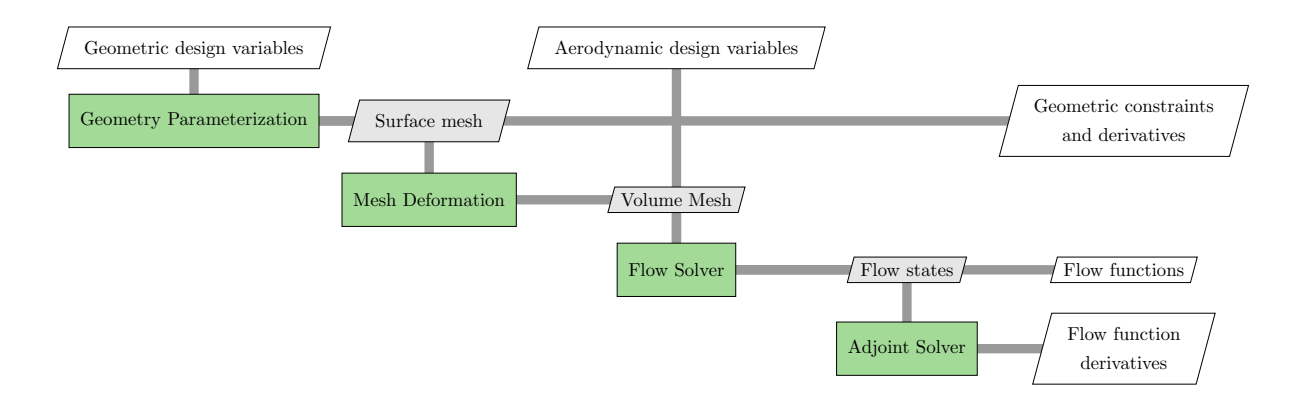


Fig. 2 Details of the wing or propeller CFD component in Fig. 1. Each CFD component has its own geometry parameterization, mesh deformation, flow solver, and adjoint solver. The wing and propeller components are coupled using OpenMDAO/MPhys.

design optimization. MPhys [32] is a recently developed derivative of OpenMDAO. MPhys facilitates the coupling of high-fidelity solvers with various disciplines. We have recently coupled our open-source discrete adjoint solver DAFoam [26, 27] into the OpenMDAO/MPhys framework for the coupled wing-propeller optimization.

Figure. 1 shows the diagram of the proposed CFD-based multi-component coupled wing-propeller optimization framework. The optimizer gives a set of propeller geometric and aerodynamic design variables, i.e., twists, chord lengths, outer radius, and rotational speed, to the "Propeller CFD" component, a high-fidelity CFD propeller model. The "Propeller CFD" component then computes the power and thrust. The thrust and outer radius are sent to the "Wing CFD" component, the power is passed back to the optimizer, and the thrust is given to the force balance component. Next, the "Wing CFD" component will use the wing geometric and propeller center design variables from the optimizer to compute the drag and lift. To consider the impact of propeller design on the wing performance, this component will also use the propeller thrust and radius from the "Propeller CFD" component and add a smoothed actuator disk force field [22] to the wing flow field. The smoothed actuator force allows us to change the propeller parameters (e.g., propeller center and outer radius) as optimization design variables for the "Wing CFD" component. The lift will be passed back to the optimizer and the drag is given to the "Force Balance" component. The "Force Balance" component will compute the difference between the propeller thrust and wing drag and send it to the optimizer as a constraint. The optimizer will then use the power as the objective function and lift and force balance as the constraints to update the design for the next iteration. Note that we do not directly control or optimize the wing drag in the coupled optimization setting. However, the optimizer will still reduce the wing drag to decrease the required propeller thrust (controlled by the force balance constraint), which eventually helps reduce the propeller power. Note that we multiply a factor to convert the wing drag to the vehicle drag, before sending its value to the force balance component.

Figure 2 shows the details of the "Wing CFD" or "Propeller CFD" component in Fig. 1. Each CFD component has its own geometry parameterization, mesh deformation, flow solver, and adjoint solver, and they are coupled in OpenMDAO/MPhys. To be more specific, the wing or propeller CFD component receives the geometric and aerodynamic design variables from the optimizer. It will then pass the geometric design variables to the geometry parameterization component (pyGeo) to update the CFD surface mesh. pyGeo [33] is an open-source free-form deformation (FFD) tool to parameterize the design surface geometry. It embeds a set of point clouds into the prescribed FFD box and can then deform the point cloud by moving the FFD coordinates. pyGeo works for structured and unstructured meshes. We generate separate FFD boxes for the wing and propeller to cover their design surfaces. Next, the updated CFD surface mesh is passed to the "Mesh Deformation" component IDWarp to compute the updated CFD volume mesh. IDWarp is an open-source mesh deformation tool that uses an inverse-distance weighting approach [34] to deform high-quality volume mesh based on the new design surface. We use IDWarp to deform the volume mesh because it is smooth and can avoid numerical noise, compared with re-generating the volume mesh. Next, the volume mesh is passed to the flow solver (OpenFOAM) to compute the converged CFD state variables and objective and constraint functions (e.g., power, thrust, drag, and lift). The converged CFD state variables are passed to the adjoint solver (DAFoam) to compute the derivatives. The above diagram works for both wing and propeller CFD components.

Figure 3 shows the OpenMDAO N2 diagram for the wing-propeller coupled optimization problem setting. Traditionally,

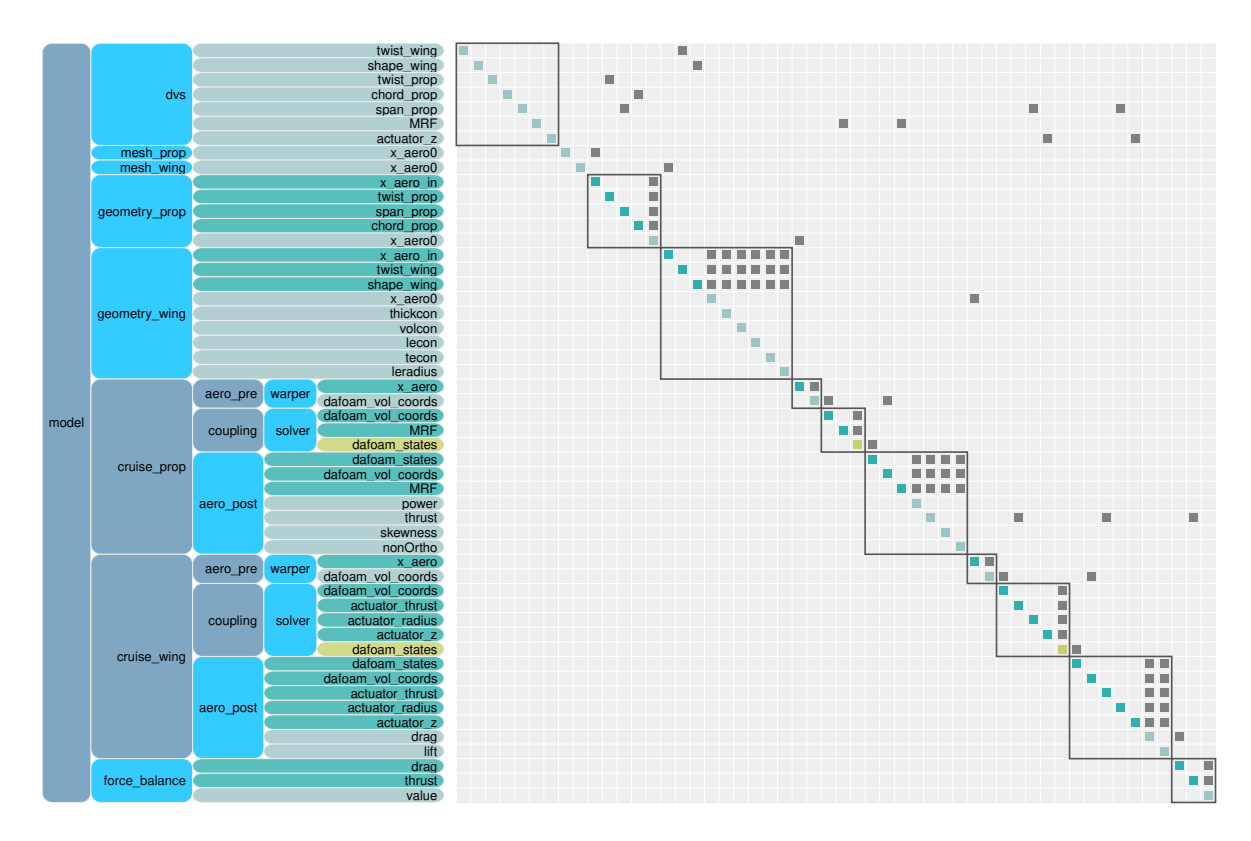


Fig. 3 OpenMDAO N2 diagram for the wing-propeller coupled optimization problem setting.

the above wing-propeller coupling is implemented in a solver-specific manner and is hard to extend. By leveraging the flexibility of OpenMDAO and MPhys, the wing-propeller coupling is implemented in a modular manner. We have incorporated DAFoam into MPhys for conducting single-component aerodynamic shape optimization. To extend it to multi-component problems, we create two copies of meshes and flow configuration files, one for the propeller and one for the wing. Then, in MPhys, we create two separate aerodynamic Builders and Scenarios to save the mesh and state variables for the wing and propeller components (cruise_prop and cruise_wing in Fig. 3). Then, we can leverage OpenMDAO's connect feature to link the coupling variables between the wing and propeller components. We use OpenMDAO's execComp feature to create the force balance component. In MPhys, we need to implement the methods to compute the output based on the input for the components shown in Figs. 2, as well as the product of the state Jacobian matrix with a given vector. OpenMADO will then use the MAUD algorithm [35] to unify the adjoint total derivative computation. Note that the wing and propeller are one-way coupled; there is no feedback from the wing to the propeller component.

III. Results

In this section, we analyze three aerodynamic optimizations: wing-only, propeller-only, and wing-propeller coupled.

A. Wing-only aerodynamic optimization with an actuator

We use the PROWIM wing planform as the baseline geometry for the wing optimization case. The unstructured CFD mesh, the FFD box, and the location and size of the actuator (disk) can be seen in Fig. 4. The wing has a rectangular shape without dihedral, whose half wingspan is 0.64 m and chord is 0.24 m, and the airfoil of it is symmetric NACA 642-015A. We place the wing with 6.981° incidence. We model the propeller as an actuator disk with 0.035 m inner and 0.12 m outer radii, which rotates at 13230 RPM in the in-board up direction. We model the flow as a compressible flow with Reynolds number 8×10^5 , the flow velocity is 50 m/s, which corresponds to a Mach number of 0.15, the temperature is 300 K, the pressure is 101.325 kPa, and the total thrust is 11.3 N with the corresponding thrust coefficient

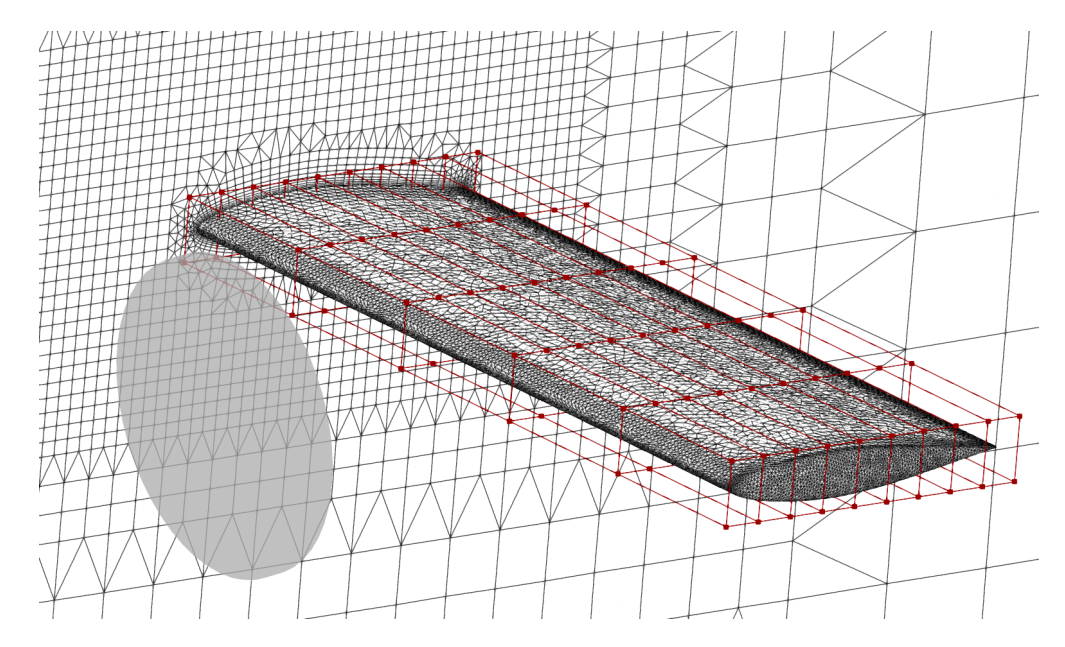


Fig. 4 PROWIM wing model, CFD mesh, and the FFD box. The red squares are the FFD control points (120 in total). The grey cylinder denotes the actuator region.

Table 1 Wing-only optimization problem formulation. We use 128 design variables and 124 constraints.

	Function/Variable	Description	Quantity
Minimize	C_D	Drag coefficient of the wing	
with respect to	$-10^{\circ} \le \gamma \le 10^{\circ}$	Twist of each FFD section	6
	$-1.0 \text{ m} \le \Delta y \le 1.0 \text{ m}$	Vertical displacements of FFD points	120
	$0.16b_{\text{half}} \le z_a \le 0.94b_{\text{half}}$	Spanwise position of actuator center	1
	$0.67 \cdot r_{2,bl} \le r_2 \le 1.17 \cdot r_{2,bl}$	Actuator outer radius	1
		Total Design Variables	128
subject to	$V_{\rm bl} \leq V$	Minimum volume constraint	1
	$0.5 \cdot t_{\rm bl} \le t \le 3 \cdot t_{\rm bl}$	Minimum thickness constraint	100
	$\Delta y_{\rm LE, upper} = -\Delta y_{\rm LE, lower}$	Fixed leading edge constraint	6
	$\Delta y_{\text{TE, upper}} = -\Delta y_{\text{TE, lower}}$	Fixed trailing edge constraint	6
	$C_L = 0.5$	Lift coefficient	1
	$r_{\text{LE, bl}} \le r_{\text{LE}} \le 3 \cdot r_{\text{LE, bl}}$	Leading edge radius constraint	10
		Total Constraint Functions	124

 $C_T \approx 0.06$. We use a computational domain, which extends 50 chord lengths in each direction from the wing leading edge on the symmetry plane. The mesh is generated using Pointwise with 660,000 cells.

We use the actuator force distribution developed by Hoekstra [36] as the base functions to calculate the axial and tangential forces of the actuator disk.

$$f_X(\hat{r}) = \hat{F}\hat{r}^m \left(\frac{a-\hat{r}}{a}\right)^n \tag{21}$$

Table 2 Wing-only optimization summary. γ_{root} is the twist at the root. The drag is reduced by 13.62%.

	Baseline Design	Optimized Design	Change %
C_D	0.03510	0.03032	-13.62
C_L	0.5	0.5	_
Optimality	1.5×10^{-2}	1.2×10^{-4}	_
Feasibility	3.7×10^{-5}	1.1×10^{-5}	_
$\gamma_{ m root}$	6.980°	3.251°	_

$$f_{\theta}(\hat{r}) = f_{x}(\hat{r}) \frac{J}{\pi \left(\frac{r}{r_{2}}\right)}$$
 (22)

where r is the radius, r_1 and r_2 are the inner and outer radii, $\hat{r} = (r - r_2)/(r_2 - r_1)$ is the normalized radius, and the parameters m = 1.0 and a = 1.0, \hat{F} is the scaling factor, which is used to equate the integral actuator source over the entire flow domain to the targeted axial force, and J is the advance ratio. Instead of directly using the above actuator force profiles, we smooth them to allow changing the actuator parameters during the optimization, as shown in our previous work [22].

The optimization problem formulation can be seen in Table 1. We use the drag coefficient as the objective function of the wing optimization case. The design variables are the twist angles of six FFD sections (γ) , vertical locations (y) of 120 FFD points, the spanwise position of the actuator center (z_a) , and the outer radius of the actuator (r_2) . We use 124 constraint functions, including lift coefficient and wing geometry constraints. The total wing volume is lower-bounded by the baseline wing volume. We sample 100 points to measure the thickness, and these thicknesses are bounded between half and three times their baseline values. We use 12 linear constraints to fix the leading and trailing edges of the wing by forcing the upper and lower FFD points at the same spanwise location to move in opposite directions. We fix the lift coefficient as 0.5. We measure the leading edge radius using the foremost 2% of the wing chord and bound it between one and three times the baseline radius.

The summary of the Wing-only optimization can be seen in Table 2. The objective function (C_D) decreased by 13.62%, where the optimality is 1.2×10^{-4} and feasibility is 1.1×10^{-5} , the C_L constraint is satisfied, and the root twist of the wing is decreased from 6.980° to 3.251°.

Fig. 5 shows the change of selected parameters during the wing-only optimization. The objective function (C_D) converges in 100 iterations. During the first 12 iterations, the C_L constraint fluctuates around the target value, but this violation is corrected by the optimizer using a penalty parameter. All FFD section twists decreased during the optimization, and the highest twist and lowest twist sections are adjacent to each other (Section-4 and Section-5, respectively; see Fig. 5 bottom left). 4 out of 100 thickness constraints are randomly selected, as shown in Fig. 5 bottom right. All of these thickness constraints stay in between their bounded values. Further details of Wing-only optimization can be found in Section III.C, where we compare the results of the wing-only and coupled wing-propeller optimizations.

B. Propeller-only aerodynamic optimization

We use the PROWIM propeller blade as the baseline geometry for the propeller-only optimization case. The propeller has 4 twisted blades, whose inner radius is 0.035 m and the outer radius is 0.12 m. The propeller rotates at 13230 RPM and the rotation direction is inboard-up; the corresponding advance ratio is 0.94. We model the flow as a compressible flow with Reynolds number 8×10^5 , the flow velocity is 50 m/s, which corresponds to a Mach number of 0.15, the temperature is 300 K, the pressure is 101.325 kPa, and the target thrust is 11.3 N. We use a cylindrical computational domain, which extends ~ 1 , ~ 2 , and ~ 2 propeller tip radii in the upstream, downstream, and spanwise directions, respectively. We use Pointwise to generate an unstructured mesh consisting of 730,000 cells. The unstructured propeller mesh slices at the root and tip of the blade (10% and 90% of the blade span, respectively), and the blade surface mesh and the FFD box can be seen in Fig. 6. We fix the first 3 layers of the FFD section to prevent the change of intersection curve between the blade and the spinner during the optimization. In order words, we allow only the top seven sections of FFD points to move.

The propeller-only optimization problem formulation can be seen in Table 3. We use the propeller shaft power (P)

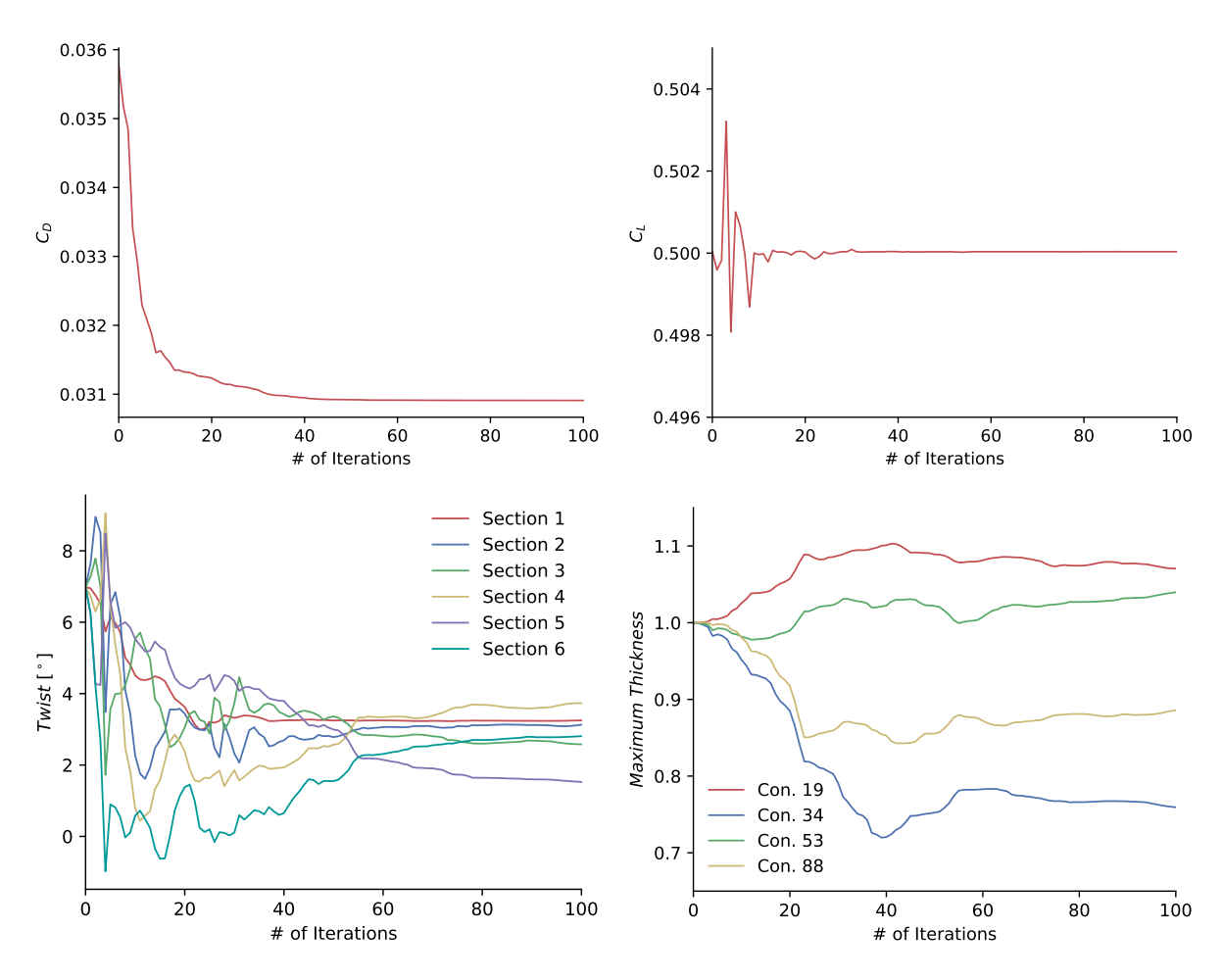


Fig. 5 Convergence of wing-only optimization parameters and constraints for the Wing-only optimization. The drag is reduced by 13.62%, and all the constraints are satisfied. Top left: C_D . Top right: C_L . Bottom left: Twists of FFD sections. Bottom right: randomly selected thickness constraints which are bounded between 0.5 and 3.0.

Table 3 Propeller-only optimization problem formulation. We use 16 design variables and 3 constraints.

	Function/Variable	Description	Quantity
Minimize	Р	Shaft power	
with respect to	$-10^{\circ} \le \gamma \le 10^{\circ}$	Twist of each FFD section	7
	$0.8 \cdot c_{\rm bl} \le \Delta c \le 1.2 \cdot c_{\rm bl}$	Chord change for each FFD section	7
	$0.67 \cdot r_{2,bl} \le r_2 \le 1.17 \cdot r_{2,bl}$	Outer radius	1
	$0.8 \cdot \omega_{\rm bl} \le \omega \le 1.2 \cdot \omega_{\rm bl}$	Rotational speed	1
		Total Design Variables	16
subject to	$T = T_{\text{target}}$	Thrust matching constraint	1
	$Q_{\text{non-ortho}} \le 75^{\circ}$	Mesh quality constraint (non-orthogonality)	1
	$Q_{\text{skewness}} \leq 5$	Mesh quality constraint (skewness)	1
		Total Constraint Functions	3

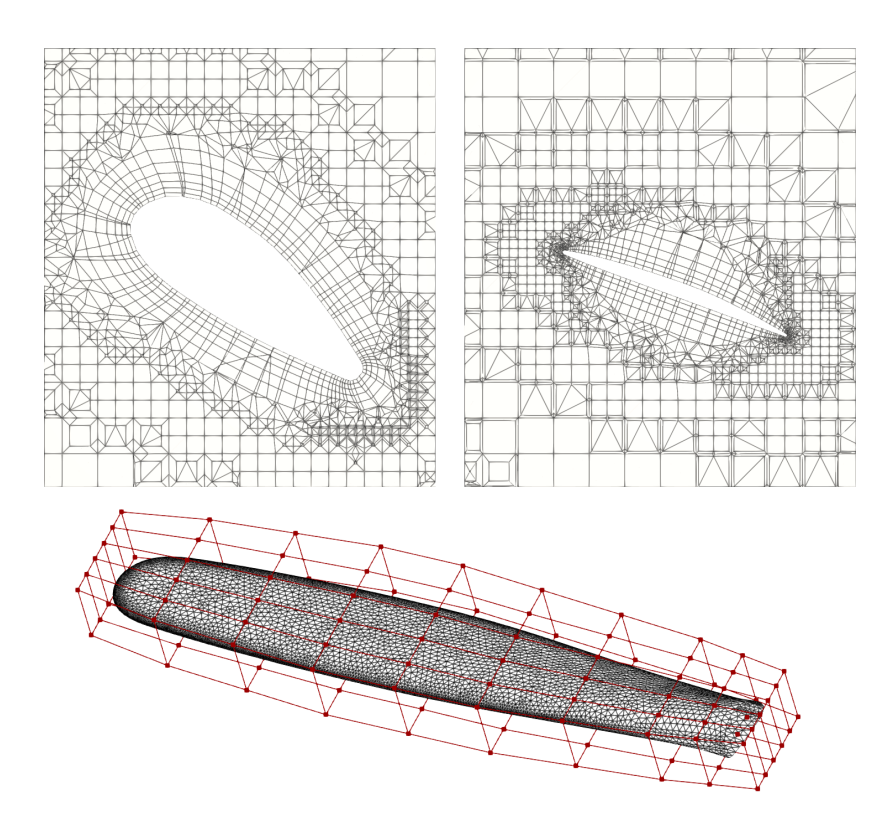


Fig. 6 Propeller mesh and FFD points. Top: Propeller mesh at the root (left) and the tip (right) sections. Bottom: Pointwise generated surface mesh of the propeller blade and the FFD points.

Table 4 Propeller-only optimization summary. 6.540% power reduction is obtained. The thrust is fixed as 11.3N. ω and r_2 are the rotation speed and outer radius, respectively.

	Baseline Design	Optimized Design	Change %
P [kW]	0.7425	0.6939	-6.540
Thrust [N]	11.30	11.30	_
C_T	0.0595	0.0881	_
ω [RPM]	13230	10680	-19.27
r ₂ [m]	0.1200	0.1211	_

as the objective function. The design variables are the twist angles (γ) and chord length (c) of seven spanwise FFD sections, the outer radius (r_2) , and the rotational speed (ω) of the propeller. We use only 3 different constraint functions. The thrust matching constraint ensures that the generated thrust equals 11.3 N. In our research, we find that the first 10 to 15 iterations of a propeller optimization are critical mesh quality. To handle this problem we use maximal non-orthogonality and skewness mesh constraints, which are upper-bounded by 75° and 5, respectively. The mesh quality values are computed using OpenFOAM's built-in checkMesh utility and DAFoam has a flexible interface to compute the constraints' derivatives with respect to the design variables through automatic differentiation.

The summary of the wing optimization can be seen in Table 4. The objective function (P) decreases by 6.540%, and the thrust (T) remains the same. The rotational speed of the propeller decreases by 19.27%, and the outer radius increases slightly.

Fig. 7 shows the convergence of selected parameters during the optimization. The optimization converged in 102 iterations. The objective function (P) converges well and decreases rapidly in the first 20 iterations. The thrust constraint fluctuates around the target value during the first 30 iterations. The effect of these thrust fluctuations on the power can be seen by comparing these two plots. We observe that only the twist of Section-1, which is the closest movable FFD

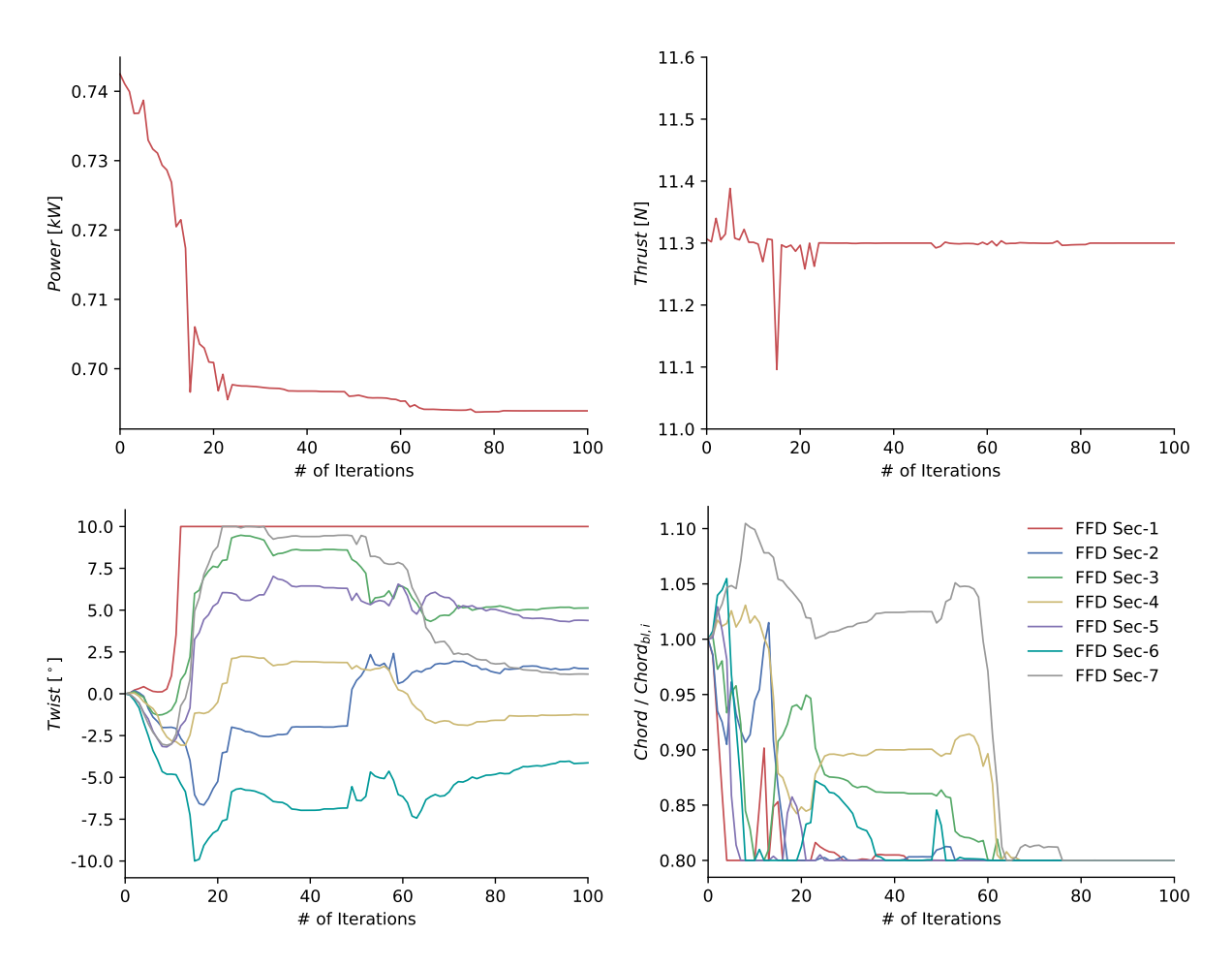


Fig. 7 Convergence of propeller-only optimization parameters and constraints for the Wing optimization. The power is reduced by 6.540%, and all the constraints are satisfied. Top left: Power. Top right: Thrust. Bottom left: Twists of FFD sections. Bottom right: Chords of FFD sections.

section to the root, reaches its bounds. Although they have different trends during the optimization, the chord lengths of all FFD sections reach their lower bounds at the end. Further details of Propeller-only optimization can be found in Section III.C, where we compare the results of propeller-only and coupled wing-propeller optimizations.

C. Coupled aerodynamic optimization

We use the above wing planform and propeller as the baseline geometry for the coupled wing-propeller optimization case. The wing and propeller geometries are defined in Secs. III.A and III.B, respectively, and the coupling method is explained in Secs. III.C. We use the same flow conditions and simulation configurations for the wing and propeller defined in Secs. III.A and III.B, respectively. The combined unstructured CFD mesh, the FFD boxes, and the effect of the existence of the propeller on the streamwise velocity can be seen in Fig. 8.

The wing-propeller coupled optimization problem formulation can be seen in Table 5. We use propeller shaft power (P) as the objective function. The wing-related design variables are the twist angles of six spanwise FFD sections (γ) and vertical locations (y) of 120 FFD points, and the propeller-related design variables are the twist angles (γ) and chord length (c) of seven spanwise propeller FFD sections, the outer radius (r_2) , and the rotational speed (ω) . We use 127 different design constraint functions. The wing-related constraints are a total wing volume constraint, 100 minimum wing thickness constraints, 6 leading edge and 6 trailing edge fixing constraints, 10 leading edge radius constraints, and a fixed lift coefficient constraint; these constraints were explained in Sec. III.A. The propeller-related constraints are two mesh quality (non-orthogonality and skewness) constraints; these constraints were explained in Sec. III.B. The last constraint is the force balance constraint. This constraint receives the thrust from the "Propeller CFD" component and

Table 5 Coupled wing-propeller optimization problem formulation. We use 143 design variables and 127 constraints.

	Function/Variable	Description	Quantity
Minimize	P	Shaft power	
with respect to	$-10^{\circ} \le \gamma_{\rm wing} \le 10^{\circ}$	Twist of each Wing FFD section	6
	$-1.0 \text{ m} \le \Delta y_{\text{wing}} \le 1.0 \text{ m}$	Vertical displacements of wing FFD points	120
	$-10^{\circ} \le \gamma_{\text{prop}} \le 10^{\circ}$	Twist of each Propeller FFD section	7
	$0.67 \cdot r_{2,bl} \le r_2^{\text{prop}} \le 1.17 \cdot r_{2,bl}$	Propeller outer radius	1
	$0.8 \cdot c_{\rm bl} \le \Delta c_{\rm prop} \le 1.2 \cdot c_{\rm bl}$	Chord change for each Propeller FFD section	7
	$0.1 \le z_p^{\text{prop}} \le 0.6$	Spanwise position of propeller center	1
	$0.8 \cdot \omega_{\rm bl} \le \omega_{\rm prop} \le 1.2 \cdot \omega_{\rm bl}$	Propeller rotational speed	1
		Total Design Variables	143
subject to	$V_{\rm bl} \leq V$	Minimum Wing volume constraint	1
	$0.5 \cdot t_{\rm bl} \le t \le 3 \cdot t_{\rm bl}$	Minimum Wing thickness constraint	100
	$\Delta y_{\text{LE, upper}} = -\Delta y_{\text{LE, lower}}$	Wing fixed leading edge constraint	6
	$\Delta y_{\text{TE, upper}} = -\Delta y_{\text{TE, lower}}$	Wing fixed trailing edge constraint	6
	$r_{\text{LE, bl}} \le r_{\text{LE}} \le 3 \cdot r_{\text{LE, bl}}$	Wing leading edge radius constraint	10
	$C_L = 0.5$	Lift coefficient	1
	Drag = Thrust	Drag - Thrust force balance constraint	1
	$Q_{\text{non-ortho}} \leq 80^{\circ}$	Propeller mesh non-orthogonality constraint	1
	$Q_{\text{skewness}} \leq 5$	Propeller mesh skewness constraint	1
		Total Constraint Functions	127

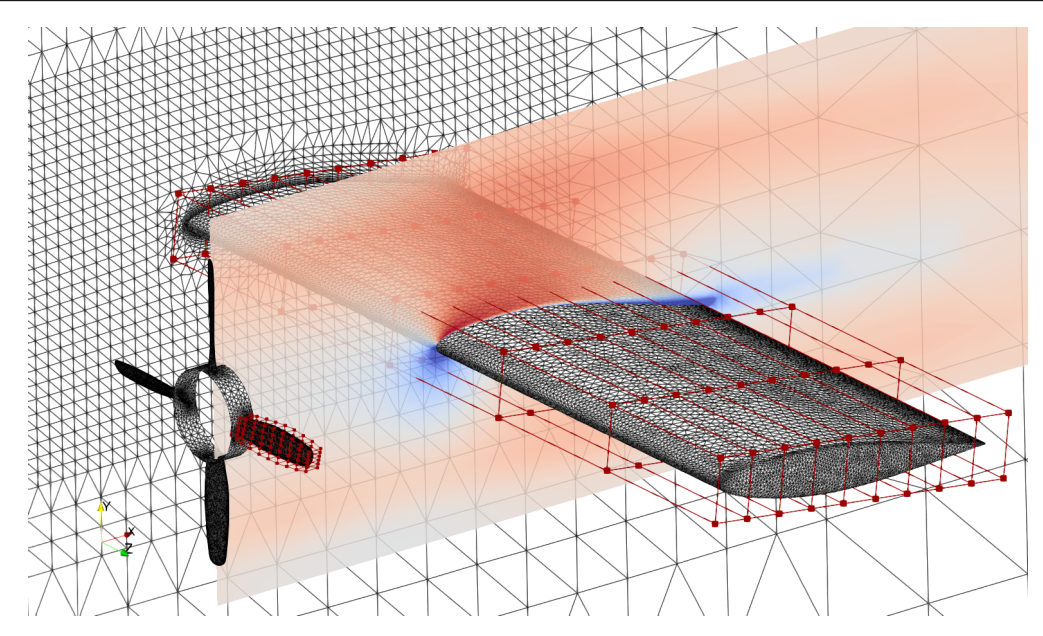


Fig. 8 Wing and propeller meshes and FFD boxes for the coupled optimization. The red squares are the FFD control points (120 for each FFD box). The streamwise velocity change caused by the propeller is also visible.

Table 6 Wing-propeller coupled optimization summary. 18.30% power reduction is obtained. ω and z_p are the rotation speed and the spanwise location of the propeller center, respectively

	Baseline Design	Optimized Design	Change %
P [kW]	0.7372	0.6023	-18.30
C_L	0.5	0.5	_
Wing drag [N]	11.30	9.745	_
Propeller thrust [N]	11.30	9.743	_
ω [RPM]	13210	10580	-19.91
z_p [m]	0.3000	0.5989	_

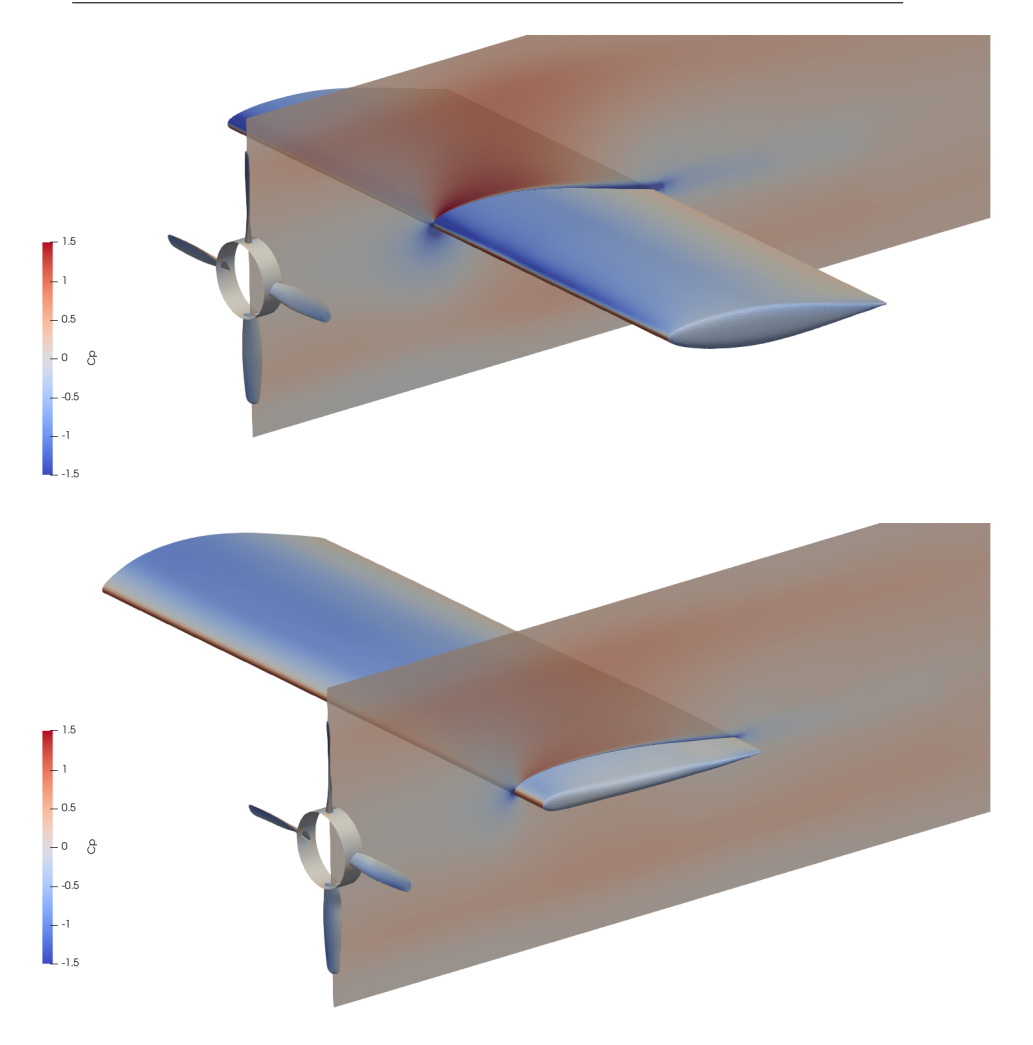


Fig. 9 C_P distribution on the baseline (top) and optimized (bottom) designs. The streamwise velocity change caused by the propeller is also visible.

lift from the "Wing CFD" component, computes their difference, and sends it to the optimizer. So the wing drag equals the propeller thrust when the optimization converges. As mentioned above, we multiply the wing drag by a factor of 1.38 for the vehicle drag, before sending it to the force balance component. Note that the "Propeller CFD" component is linked to the actuator disk profiles in the "Wing CFD" component. In other words, we will change the actuator disk profiles shown in Eqs. 21 and 22 based on the "Propeller CFD" component's thrust and outer radius.

The summary of the coupled optimization can be seen in Table 6. The objective function (P) decreased by 18.30%,

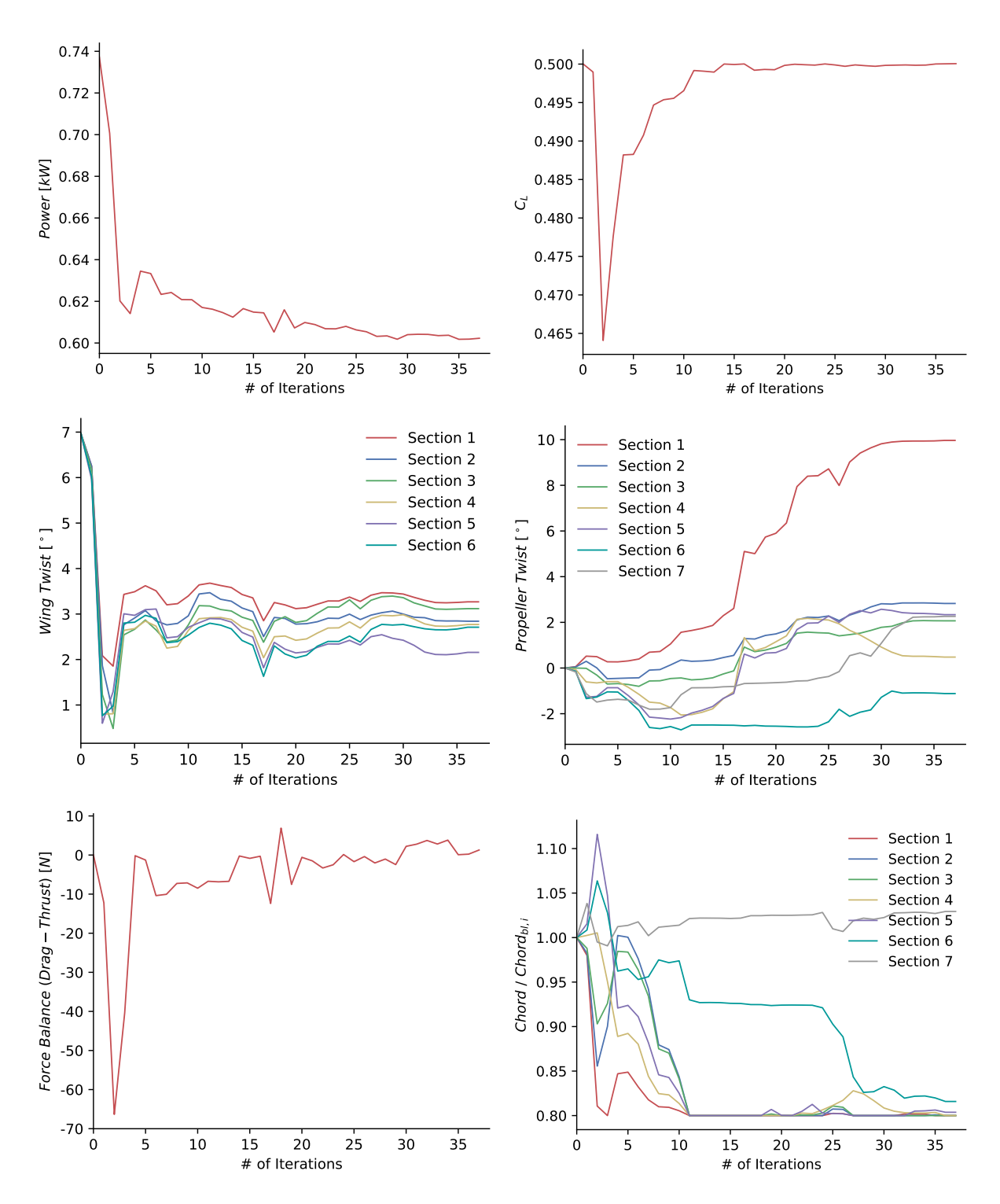


Fig. 10 Convergence of optimization parameters and constraints for the wing-propeller coupled optimization. The power is reduced by 18.30%, and all the constraints are satisfied. Top left: Power. Top right: C_L . Mid Left: Twists of Propeller FFD sections. Mid Right: Twists of Wing FFD sections. Bottom Left: Force balance between wing drag and propeller thrust. Bottom Right: Chords of Propeller FFD sections

which is nearly three times of the Propeller-only Optimization. The C_L remains the same during the optimization. Moreover, the force balance constraint is satisfied, i.e., the wing drag and propeller thrust are equal in both the baseline

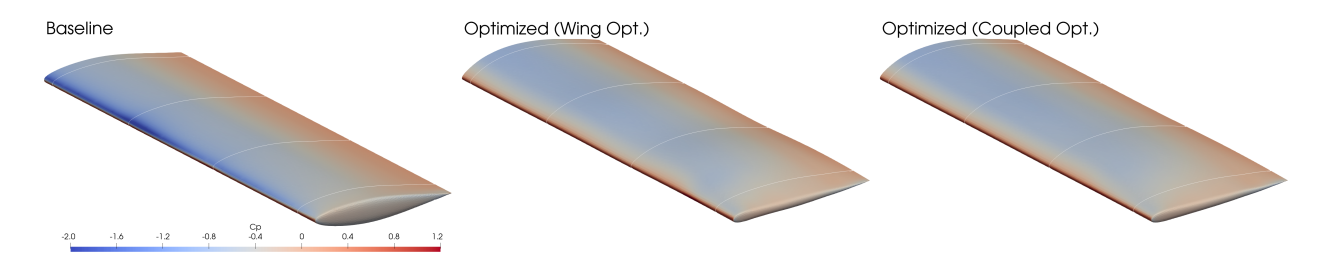


Fig. 11 Pressure contours for the baseline (left), Wing-only optimization (mid), and wing-propeller coupled optimization (right) designs of the wing. The white profiles denote the four wing sections for plotting the C_p distributions.

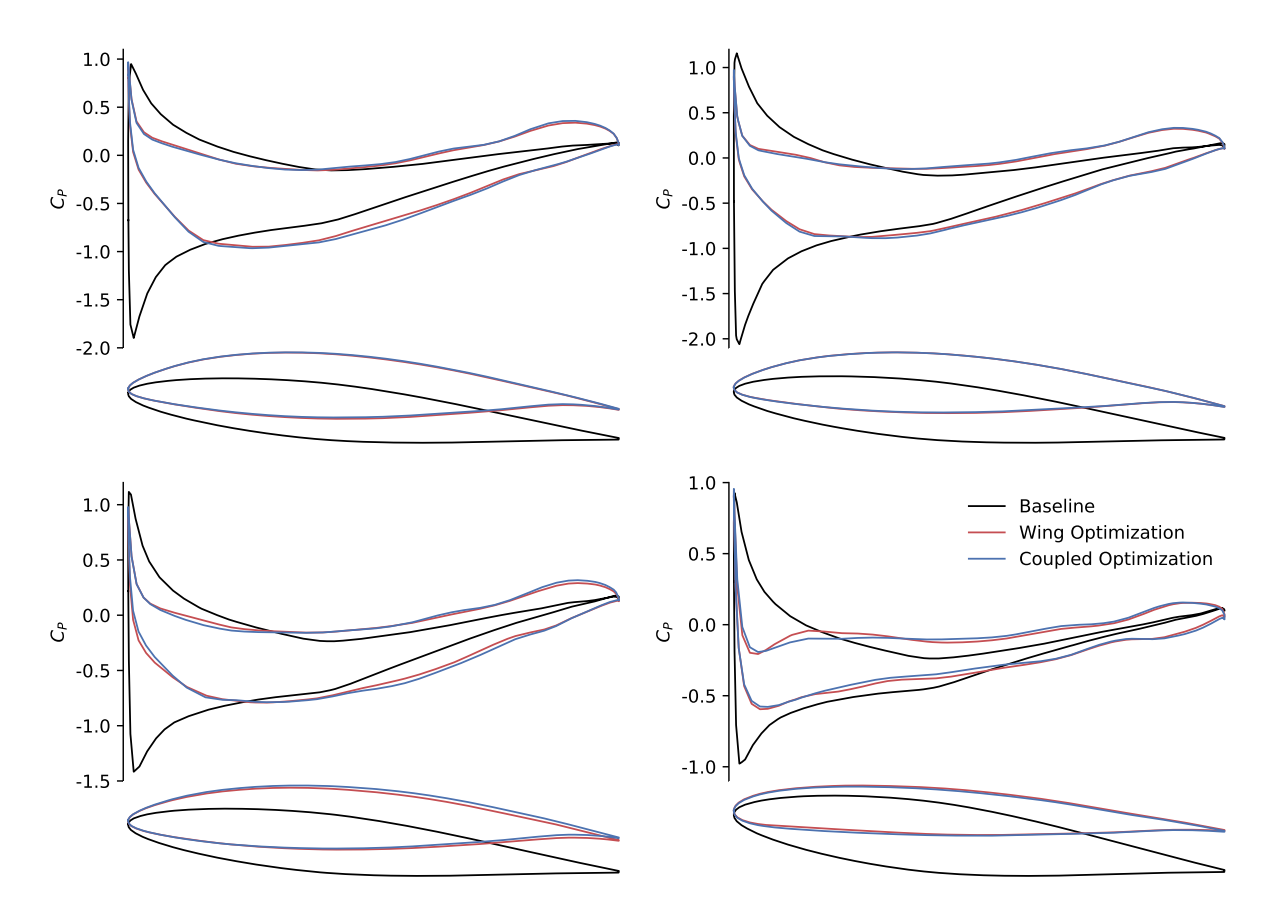


Fig. 12 Change of C_p distribution and airfoil shape at different wing sections for the wing. Top left: 3% span. Top right: 31% span. Bottom left: 63% span. Bottom right: 94% span. The baseline, Wing Optimization optimized design, and Coupled Optimization optimized design are denoted in black, red, and blue, respectively.

and optimized designs. As expected, both wing drag and propeller thrust reduce in the optimized design for reducing the propeller power consumption. The rotational speed of the propeller decreases by 19.91%, which is close to the Propeller-only optimization. The propeller moves from around the center of the wing (0.3) to the tip of the wing (0.5989) in the spanwise direction, which is in agreement with our previous finding [22]. A more detailed comparison can be found in Fig. 9, where the C_P distribution is plotted for the baseline and optimized wing-propeller configurations. Fig. 10 shows the change of selected parameters during the coupled optimization. The objective function (P) converges in 37 iterations. During the first few iterations, the C_L constraint decreases rapidly, but this violation is corrected by the optimizer. The twists of spanwise wing FFD sections and the force balance constraint have a similar fashion; they steeply decrease in the first few iterations.

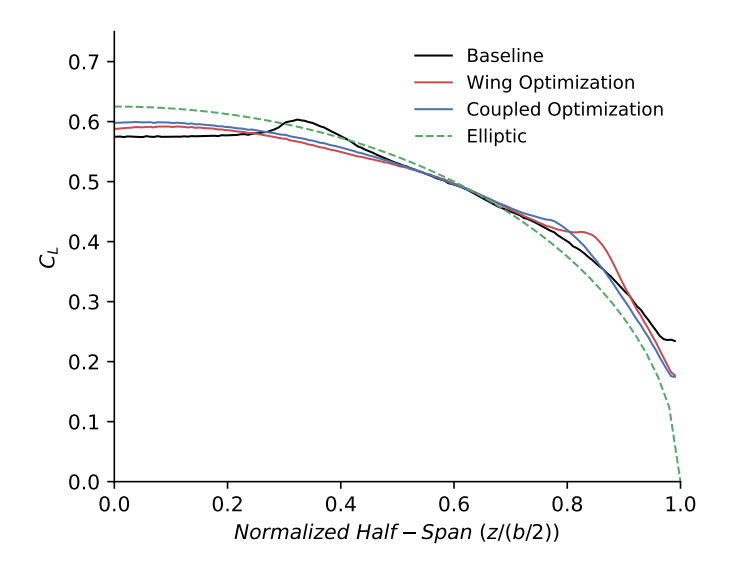


Fig. 13 Comparison of C_L distribution along the wing span of the baseline and optimized designs.

Fig. 11 shows the baseline and optimized wing geometries and four spanwise sections, which we use to investigate the change of C_p distribution and sectional airfoil shape. As shown in Fig. 12, the symmetric airfoil of the baseline geometry turns into a cambered airfoil and gets thinner at the tip, similar to what we observed in our previous study [22]. This change in the airfoil shape reduces the wing sectional pitch angles and increases aerodynamic performance. The wing airfoil profiles are similar between the Wing-only and coupled optimizations. Compared with the baseline design, the optimized designs have a smoother wing loading, i.e., the high loading in the baseline design is changed to a more evenly distributed loading in the optimized designs.

Fig. 13 shows the spanwise C_L distribution for the baseline and optimized wing designs. Neither baseline nor optimized wing designs match the theoretical elliptical lift distribution because of the existence of the actuator/propeller. The actuator/propeller distorts the lift distribution. Although the center locations of the actuator and the propeller are nearly the same for the Wing-only and coupled optimized designs, the disturbance generated by the coupled optimization is weaker than the Wing-only optimization.

Fig. 14 shows the airfoil profiles of baseline and optimized propeller blades at different spanwise sections. Compared with the baseline design, both optimized designs have higher twist angles (higher incidence) except for sections closer to their tips, where their twists are less than the baseline design. Overall, the optimized shapes are similar between the propeller-only and coupled optimizations, except that: (1) the twist range of the coupled optimization's blade is slightly smaller, and (2) the propeller Optimization's blade chord is slightly shorter around the tip.

Fig. 15 shows the comparison of pressure profiles at four different spanwise locations. As expected, the pressure load increases along the span, and the thrust of the root sections of the propeller is nearly negligible. Compared with the wing case, the propeller-only and coupled optimizations exhibit larger differences in their pressure distributions. The coupled optimization's blade loading is less than the propeller-only case at all sections. This is consistent with what we observed for their twist angle difference. The coupled optimization's sectional twists are higher than the propeller-only optimization.

Fig. 16 shows the spanwise thrust distribution of baseline and optimized designs. The peak thrusts of both optimized propellers are decreased and shifted to the blade roots while satisfying the target thrust constraint. Another important difference is around the root section of the optimized designs, where we observe a small region with negative thrust.

IV. Conclusion

In this paper, we conduct multi-component aerodynamic optimizations for wing-propeller coupling. We use a high-fidelity CFD solver (OpenFOAM) to simulate the wing and propeller with separate meshes. We then use the discrete adjoint approach to compute the derivatives of objective and constraint functions with respect to a large number of design variables and constraints using DAFoam. The adjoint method allows us to have large design freedom for performance

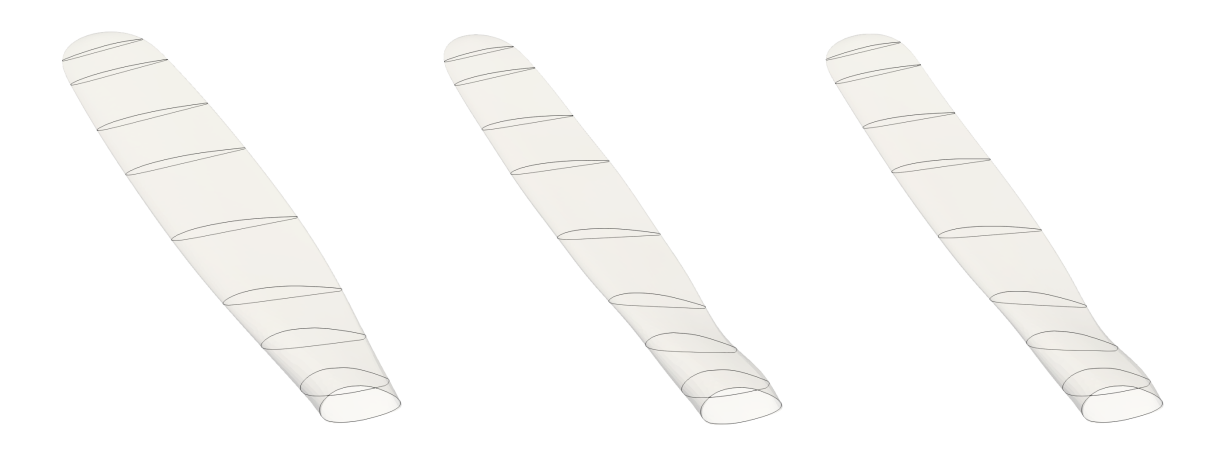


Fig. 14 Comparison of airfoil profiles on the baseline (left), Propeller-only optimization (mid), and propeller-wing coupled optimization (right) designs at different spanwise sections.

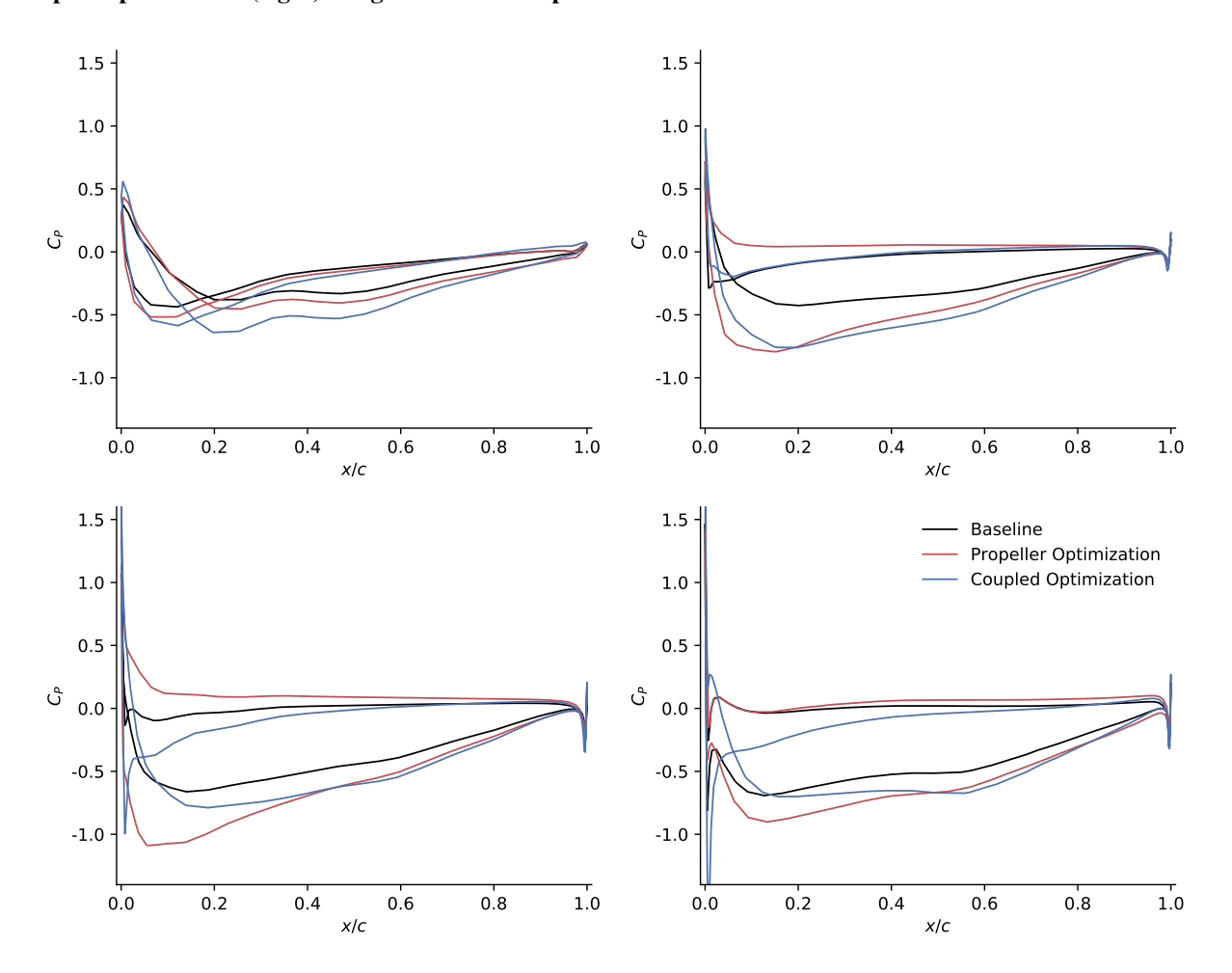


Fig. 15 Change of C_p distribution at different propeller blade sections. Top left: 10% blade span. Top right: 40% blade span. Bottom left: 70% blade span. Bottom right: 90% blade span. The baseline, Propeller Optimization optimized design, and Coupled Optimization optimized design are denoted in black, red, and blue, respectively.

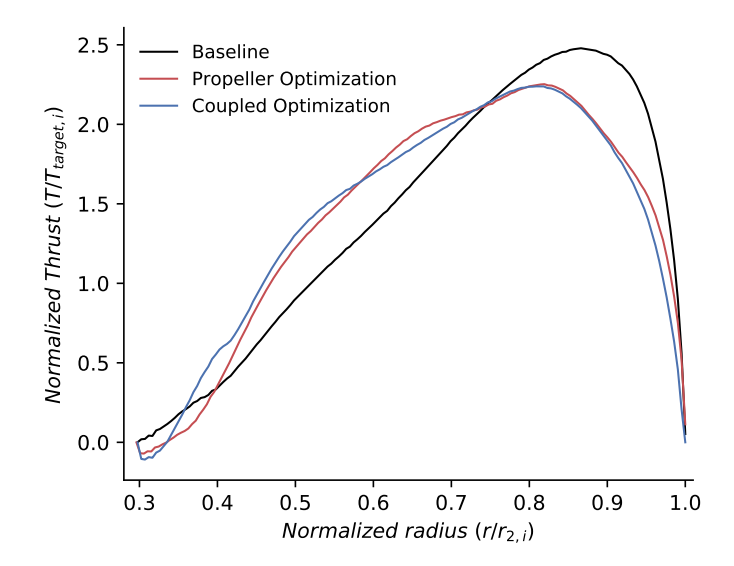


Fig. 16 Comparison of thrust distribution along the propeller blade span of the baseline and optimized designs.

improvement. The wing-propeller coupling is done by extracting the CFD propeller force and outer radius and adding the corresponding actuator source term into the CFD wing flow field under the OpenMDAO/MPhys framework. The objective function is the propeller power consumption, and the design variables are the wing shape and twist, propeller center, twist, chord, outer radius, and rotation speed. We impose a force balance constraint to ensure that the propeller thrust equals the wing drag. We also impose other aerodynamic and geometric constraints, such as lift, volume, and thickness for the wing.

Our aerodynamic optimization results show that the coupled wing-propeller optimization exhibits more performance improvement than optimizing the wing and propeller separately. To be more specific, the coupled optimization achieves 18.3% power reduction, while the propeller-only setting achieves only 6.54% power reduction. The main driving mechanism is that the wing drag is optimized in the coupled optimization; therefore, the required propeller thrust is reduced, which eventually contributes to lower power consumption.

This study has the potential to significantly reduce the time period for designing high-performance wing and propeller coupling systems. We are currently working on transferring the thrust and tangential force profiles directly from the propeller CFD component, instead of assuming an idealized actuator force profile, and will report more results in our future work.

Acknowledgments

Ping He acknowledges the funding supported by the National Science Foundation under Grant Number 2223676. The computations were partially done in the Extreme Science and Engineering Discovery Environment (XSEDE), which is supported by National Science Foundation Grant number ACI-1548562.

References

- [1] Gipson, L., "Advanced Air Mobility Mission Overview," https://www.nasa.gov/aam/overview/, October 7, 2021. Accessed: 2022-01-30.
- [2] Patterson, M. D., Daskilewicz, M. J., , and German, B., "Conceptual Design of Electric Aircraft with Distributed Propellers: Multidisciplinary Analysis Needs and Aerodynamic Modeling Development," *52nd Aerospace Sciences Meeting*, AIAA Paper 2014-0534, 2014. https://doi.org/10.2514/6.2014-0534.
- [3] Moore, M. D., and Fredericks, B., "Misconceptions of Electric Aircraft and their Emerging Aviation Markets," *52nd Aerospace Sciences Meeting*, AIAA Paper 2014-0535, 2014. https://doi.org/10.2514/6.2014-0535.
- [4] Stoll, A. M., Bevirt, J. B., Moore, F., M. D., J., W., and Borer, N. K., "Drag Reduction Through Distributed Electric

- Propulsion," 14th AIAA Aviation Technology, Integration, and Operations Conference, AIAA Paper 2014-2851, 2014. https://doi.org/10.2514/6.2014-2851.
- [5] Rakshith, B. R., Deshpande, S. M., Narasimha, R., and Praveen, C., "Optimal Low-Drag Wing Planforms for Tractor-Configuration Propeller-Driven Aircraft," *Journal of Aircraft*, Vol. 52, No. 6, 2015, pp. 1791–1801. https://doi.org/10.2514/1. C032997.
- [6] Deere, K. A., Viken, J. K., Viken, S., Carter, M. B., Wiese, M., and Farr, N., "Computational Analysis of a Wing Designed for the X-57 Distributed Electric Propulsion Aircraft," 35th AIAA Applied Aerodynamics Conference, AIAA Paper 2017-3923, 2017. https://doi.org/10.2514/6.2017-3923.
- [7] Hwang, J. T., and Ning, A., "Large-Scale Multidisciplinary Optimization of an Electric Aircraft for On-Demand Mobility," 2018 AIAA/ASCE/AHS/ASC Structures, Structural Dynamics, and Materials Conference, AIAA Paper 2018-1384, 2018. https://doi.org/10.2514/6.2018-1384.
- [8] Brelje, B. J., and Martins, J. R. R. A., "Electric, Hybrid, and Turboelectric Fixed-Wing Aircraft: A Review of Concepts, Models, and Design Approaches," *Progress in Aerospace Sciences*, Vol. 104, 2019, pp. 1–19. https://doi.org/10.1016/j.paerosci.2018.06. 004.
- [9] Moore, K. R., and Ning, A., "Takeoff and Performance Trade-Offs of Retrofit Distributed Electric Propulsion for Urban Transport," *Journal of Aircraft*, Vol. 56, No. 5, 2019, pp. 1880–1892. https://doi.org/10.2514/1.c035321.
- [10] de Vries, R., Hoogreef, M., and Vos, R., "Preliminary Sizing of a Hybrid-Electric Passenger Aircraft Featuring Over-the-Wing Distributed-Propulsion," AIAA Scitech 2019 Forum, AIAA Paper 2019-1811, 2019. https://doi.org/10.2514/6.2019-1811.
- [11] Palaia, G., Salem, K. A., Cipolla, V., Binante, V., and Zanetti, D., "A Conceptual Design Methodology for e-VTOL Aircraft for Urban Air Mobility," *Applied Sciences*, Vol. 11, No. 22, 2021, p. 10815. https://doi.org/10.3390/app112210815.
- [12] Zhang, T., and Barakos, G. N., "High-fidelity numerical analysis and optimisation of ducted propeller aerodynamics and acoustics," *Aerospace Science and Technology*, Vol. 113, 2021, p. 106708. https://doi.org/10.1016/j.ast.2021.106708.
- [13] Hu, Y., xiang Qing, J., Liu, Z. H., Conrad, Z. J., Cao, J. N., and Zhang, X. P., "Hovering efficiency optimization of the ducted propeller with weight penalty taken into account," *Aerospace Science and Technology*, Vol. 117, 2021, p. 106937. https://doi.org/10.1016/j.ast.2021.106937.
- [14] van Arnhem, N., de Vries, R., Sinnige, T., Vos, R., and Veldhuis, L. L. M., "Aerodynamic Performance and Static Stability Characteristics of Aircraft with Tail-Mounted Propellers," *Journal of Aircraft*, Vol. 59, No. 2, 2022, pp. 415–432. https://doi.org/10.2514/1.C036338.
- [15] Zhang, T., and Barakos, G. N., "High-fidelity numerical investigations of rotor-propeller aerodynamic interactions," *Aerospace Science and Technology*, Vol. 124, 2022, p. 107517. https://doi.org/10.1016/j.ast.2022.107517.
- [16] Zanotti, A., and Algarotti, D., "Aerodynamic interaction between tandem overlapping propellers in eVTOL airplane mode flight condition," *Aerospace Science and Technology*, Vol. 124, 2022, p. 107518. https://doi.org/10.1016/j.ast.2022.107518.
- [17] Alba, C., Elham, A., German, B. J., , and Veldhuis, L. L. M., "A Surrogate-Based Multi-Disciplinary Design Optimization Framework Modeling Wing-Propeller Interaction," *Aerospace Science and Technology*, Vol. 78, 2018, pp. 721–733. https://doi.org/10.1016/j.ast.2018.05.002.
- [18] Stokkermans, T. C. A., van Arnhem, N., Sinnige, T., and Veldhuis, L. L. M., "Validation and Comparison of RANS Propeller Modeling Methods for Tip-Mounted Applications," AIAA Journal, Vol. 57, 2019, pp. 566–580. https://doi.org/10.2514/1. J057398.
- [19] Stokkermans, T., Veldhuis, L., Soemarwoto, B., Fukari, R., and Eglin, P., "Breakdown of aerodynamic interactions for the lateral rotors on a compound helicopter," *Aerospace Science and Technology*, Vol. 101, 2020, p. 105845. https://doi.org/10.1016/j.ast.2020.105845.
- [20] de Vries, R., van Arnhem, N., Sinnige, T., Vos, R., and Veldhuis, L. L. M., "Aerodynamic interaction between propellers of a distributed-propulsion system in forward flight," *Aerospace Science and Technology*, Vol. 118, 2021, p. 107009. https://doi.org/10.1016/j.ast.2021.107009.
- [21] Chauhan, S. S., and Martins, J. R. R. A., "RANS-based Aerodynamic Shape Optimization of a Wing Considering Propeller–Wing Interaction," *Journal of Aircraft*, Vol. 58, 2021, pp. 497–513. https://doi.org/10.2514/1.C035991.

- [22] Koyuncuoglu, H. U., and He, P., "Simultaneous wing shape and actuator parameter optimization using the adjoint method," *Aerospace Science and Technology*, Vol. 130, 2022, p. 107876. https://doi.org/https://doi.org/10.1016/j.ast.2022.107876.
- [23] Spalart, P., and Allmaras, S., "A One-Equation Turbulence Model for Aerodynamic Flows," 30th Aerospace Sciences Meetingand Exhibit, AIAA Paper 1992-439, 1992. https://doi.org/org/10.2514/6.1992-439.
- [24] Patankar, S. V., and Spalding, D. B., "A calculation procedure for heat, mass and momentum transfer in three dimensional parabolic flows," *International Journal of Heat and Mass Transfer*, Vol. 15, No. 10, 1972, pp. 1787–1806. https://doi.org/10.1016/0017-9310(72)90054-3.
- [25] Rhie, C., and Chow, W. L., "Numerical study of the turbulent flow past an airfoil with trailing edge separation," *AIAA Journal*, Vol. 21, No. 11, 1983, pp. 1525–1532. https://doi.org/10.2514/3.8284.
- [26] He, P., Mader, C. A., Martins, J. R. R. A., and Maki, K. J., "An Aerodynamic Design Optimization Framework Using a Discrete Adjoint Approach with OpenFOAM," *Computers & Fluids*, Vol. 168, 2018, pp. 285–303. https://doi.org/10.1016/j.compfluid. 2018.04.012.
- [27] He, P., Mader, C. A., Martins, J. R. R. A., and Maki, K. J., "DAFoam: An Open-Source Adjoint Framework for Multidisciplinary Design Optimization with OpenFOAM," AIAA Journal, Vol. 58, No. 3, 2020, pp. 1304–1319. https://doi.org/10.2514/1.J058853.
- [28] "DAFoam Documentation," https://dafoam.github.io, April 20, 2022. Accessed: 2022-04-21.
- [29] Kenway, G. K. W., Mader, C. A., He, P., and Martins, J. R. R. A., "Effective adjoint approaches for computational fluid dynamics," *Progress in Aerospace Sciences*, Vol. 110, 2019, p. 100542. https://doi.org/10.1016/j.paerosci.2019.05.002.
- [30] Balay, S., Abhyankar, S., Adams, M. F., Brown, J., Brune, P., Buschelman, K., Dalcin, L., Dener, A., Eijkhout, V., Gropp, W. D., Kaushik, D., Knepley, M. G., May, D. A., McInnes, L. C., Mills, R. T., Munson, T., Rupp, K., Sanan, P., Smith, B. F., Zampini, S., Zhang, H., and Zhang, H., "PETSc Users Manual," *Tech. Rep. ANL-95/11 Revision 3.10*, Argonne National Laboratory, 2018. https://doi.org/10.2172/1483828.
- [31] Gray, J. S., Hwang, J. T., Martins, J. R. R. A., Moore, K. T., and Naylor, B. A., "OpenMDAO: An open-source framework for multidisciplinary design, analysis, and optimization," *Structural and Multidisciplinary Optimization*, Vol. 59, No. 4, 2019, pp. 1075–1104. https://doi.org/10.1007/s00158-019-02211-z.
- [32] "Mphys code," https://github.com/OpenMDAO/mphys, 2022. Accessed: 2023-01-01.
- [33] Kenway, G. K. W., Kennedy, G. J., and Martins, J. R. R. A., "A CAD-Free Approach to High-Fidelity Aerostructural Optimization," *Proceedings of the 13th AIAA/ISSMO Multidisciplinary Analysis Optimization Conference*, Fort Worth, TX, 2010. AIAA 2010-9231.
- [34] Secco, N. R., Kenway, G. K., He, P., Mader, C., and Martins, J. R., "Efficient mesh generation and deformation for aerodynamic shape optimization," *AIAA Journal*, Vol. 59, No. 4, 2021, pp. 1151–1168. https://doi.org/10.2514/1.J059491.
- [35] Martins, J. R., and Hwang, J. T., "Review and unification of methods for computing derivatives of multidisciplinary computational models," AIAA journal, Vol. 51, No. 11, 2013, pp. 2582–2599.
- [36] Hoekstra, M., "A RANS-based analysis tool for ducted propeller systems in open water condition," *International Shipbuilding Progress*, Vol. 53, 2006, pp. 205–227.